A Parallel High-Order Flux Reconstruction Solver on Unstructured Grids: Implementation and Performance Analysis

Yifan Wang*, Fuzhen Chen* and Fan Liu*,**
Corresponding author: liufan@nwpu.edu.cn
* Northwestern Polytechnical University, 1Donxiang Road, Xi'an 710072, China

Abstract: This paper presents a parallel solver for unstructured grids based on the Flux Reconstruction / Correction Procedure via Reconstruction (FR/CPR) method. The solver is implemented in Fortran and incorporates multiple limiters, including TVB, Modal, KXRCF, and CKXRCF, to capture discontinuities while preserving high-order accuracy in smooth regions. The algorithm is first validated on the one-dimensional SOD shock tube problem, where high-order polynomial Gibbs phenomena are observed near the shock. Despite the absence of shock-capturing techniques, the FR/CPR method accurately reproduces the flow field with sufficient degrees of freedom. Two two-dimensional benchmark cases—double Mach reflection and shock–vortex interaction—are then simulated to evaluate the performance of the four limiters. All limiters successfully capture key features such as shock waves, slip lines, and vortex structures arising from Kelvin–Helmholtz instability. Differences in the marking of problematic cells are noted, but overall flow-field characteristics remain consistent. The results demonstrate that the FR/CPR method, combined with appropriate limiters, provides a robust and accurate framework for high-order CFD simulations on unstructured grids.

Keywords: Flux Reconstruction, Computational Fluid Dynamics, High-order methods, Limiter.

1. Introduction

The development of high-order methods for solving the Navier-Stokes equations on unstructured grids represents a significant advancement in computational fluid dynamics over the past two decades. Compared to first- or second-order schemes, high-order methods are capable of achieving higher accuracy with less computational time in scale-resolving simulations, an advantage that has been consistently demonstrated in multiple international workshops on high-order CFD methods[1]. Among the most widely adopted high-order approaches on unstructured grids is the Discontinuous Galerkin (DG) method[2]. Other high-order methodologies include the spectral difference method[3, 4], the spectral volume method[5, 6], and the Flux Reconstruction/Correction Procedure via Reconstruction (FR/CPR) method[7, 8], all of which employ the same solution space as the discontinuous Galerkin method.

This study employs the Flux Reconstruction/Correction Procedure via Reconstruction approach. Initially formulated for structured grids, the method has since been extended to simplex and hybrid unstructured grids[9, 10]. In recent years, it has attracted considerable attention, and its development has been documented in several review articles[11]. This paper presents a parallel solver for unstructured grids based on the FR/CPR method, implemented in Fortran. Multiple limiters are incorporated, and their computational efficiency is systematically evaluated and compared through numerical verification cases.

2. Algorithm of FR/CPR Method

Consider the Euler equations for inviscid flow:

$$\frac{\partial \mathbf{V}}{\partial t} + \nabla \cdot \mathbf{F}(Q) = 0 \tag{1}$$

where $Q = [\rho, \rho u, \rho v, \rho w, \rho \mathbf{E}]^T$ are the conservative variables; ρ is density, u, v, w are the velocity components in each spatial coordianate direction; $\mathbf{E}$ is the specific total energy; and $\mathbf{F}(Q)$ are the inviscid fluxes, Assume that the computational domain Ω is discretized into N nonoverlapping elements $\{\Omega_i\}_{i=1}^N$. In each element Ω_i, solution $\mathbf{V}$ is approximated by a polynomial of order P, written as $v_n^d = v_n^d(x,t)$. Flux $\mathbf{F}(Q)$ is approximated by a polynomial of order $P+1$, written as $f_n^C = f_n^C(x,t)$, then we can get

$$v^d = \sum_{n=1}^{N} v_n^d \approx v, \quad f^C = \sum_{n=1}^{N} f_n^C \approx f \tag{2}$$

where u^d does not need to be continuous at each element surface, but f^C has to be continous at each element surface.

Then we transform the mesh element Ω_n from the physical domain to the standard element in the computational domain Ω_S:

$$\epsilon = \Gamma_n(x) = -1 + 2\left(\frac{x - x_n}{x_{n+1} - x_n}\right) \tag{3}$$

after transformation from the physical domain to the computational domain, the variable u_n^d defined on the grid cell Ω_n can be obtained by solving the transformation equation defined on the standard cell Ω_S:

$$\bar{u}_n^d + \nabla_\epsilon \bar{f}^C = 0 \tag{4}$$

where $\bar{u}_n^d$ can be obtain by Lagrange interpolation:

$$\bar{u}_n^d = \sum_{i=0}^{P} \bar{u}_{n,i}^d l_i \tag{5}$$

where

$$l_i = \prod_{j=0, j\neq i} \left(\frac{\epsilon - \epsilon_j}{\epsilon_i - \epsilon_j}\right) \tag{6}$$

Similarly, $\bar{f}_n^d$ can be written as:

$$\bar{f}_n^d = \sum_{i=0}^{P} \bar{f}_{n,i}^d l_i \tag{7}$$

For Euler equation, numerical interface fluxes are often computed using an approximate Riemann solver. Let the numerical interface fluxes obtained at the left and right ends of the standard element Ω_S be denoted as $\bar{f}_{n,L}^d$, $\bar{f}_{n,R}^d$, and let the approximate Riemann flux solver be denoted as R. Then, the numerical interface flux is given by the following formula:

$$\begin{aligned} \bar{f}_{n,L}^d &= R(\bar{u}_{n-1,R}^d, \bar{u}_{n,L}^d, \mathbf{n}_{n,L}) \\ \bar{f}_{n,R}^d &= R(\bar{u}_{n,R}^d, \bar{u}_{n+1,L}^d, \mathbf{n}_{n,R}) \end{aligned} \tag{8}$$

where $\mathbf{n}_{n,L}$ and $\mathbf{n}_{n,R}$ are the normal vector at the element interface.

Finally, we can construct the $(P+1)$-th order corrected flux polynomial $\hat{f}_n^\delta$ and add it to the discontinuous flux polynomial $\hat{f}_n^d$ to obtain the $(P+1)$-th order continuous flux polynomial $\hat{f}_n^C$. The requirement for the corrected flux polynomial $\hat{f}_n^{\delta}$ is that its values at the element interfaces equal the differences between the numerical interface fluxes $\hat{f}_n^{I,L}$, $\hat{f}_n^{I,R}$ and the discontinuous fluxes $\hat{f}_n^{d,L}$, $\hat{f}_n^{d,R}$ respectively. Meanwhile, the corrected flux polynomial $\hat{f}_n^{\delta}$ in the standard element should be approximately zero in some sense. To satisfy the above requirements, first define on Ω_S the $(P+1)$-th order corrected polynomials $g_L = g_L(\varepsilon)$, $g_R = g_R(\varepsilon)$, which are approximately zero in some sense and satisfy the following conditions:

$$\begin{aligned} &g_L(-1) = 1, g_L(1) = 0 \\ &g_R(-1) = 0, g_R(1) = 1 \\ &g_L(\varepsilon) = g_R(-\varepsilon) \end{aligned} \tag{9}$$

Different correction polynomials g_L and g_R endow the resulting flux reconstruction method with different accuracy and stability. In this sense, the flux reconstruction method is a class of methods. The following lists two feasible correction polynomials of order $(P+1)$.

$$\begin{aligned} g_{L,DG} &= R_{R,K} \\ g_L(2) &= \frac{K-1}{2K-1} R_{R,K} + \frac{K}{2K-1} R_{R,K-1} \\ R_{R,K} &= \frac{(-1)^K}{2}(\mathcal{L}_K - \mathcal{L}_{K-1}) \end{aligned} \tag{10}$$

where $K = (P+1)$, L_K is the Legendre polynomial of degree K, and g_R can be obtained by transforming the correction polynomial property equation, When the correction polynomial is taken as $g_{L,DG}$, the resulting flux reconstruction method is equivalent to the DG method for equations with a linear flux. The correction polynomial $g_{L,2}$ leads to corrections that are confined only to the boundaries, providing good numerical stability.

The form of the corrected flux polynomial $\hat{f}_n^{\delta}$ is as follows:

$$\hat{f}_n^{\delta} = ((\hat{f})_{n,L}^I - (\hat{f})_{n,L}^d) g_L + ((\hat{f})_{n,R}^I - (\hat{f})_{n,R}^d) g_R \tag{11}$$

and its derivative on Ω_S is as follows:

$$\nabla_{\varepsilon} \hat{f}_n^d(\varepsilon_i) = ((\hat{f})_{n,L}^I - (\hat{f})_{n,L}^d) \frac{dg_L}{d\varepsilon}(\varepsilon_i) + ((\hat{f})_{n,R}^I - (\hat{f})_{n,R}^d) \frac{dg_R}{d\varepsilon}(\varepsilon_i) \tag{12}$$

At the solution point ε_i, the divergence of the continuous flux polynomial $\hat{f}_n^C$ is:

$$\nabla_{\varepsilon} \hat{f}_n^C(\varepsilon_i) = \nabla_{\varepsilon} \hat{f}_n^d(\varepsilon_i) + \nabla_{\varepsilon} \hat{f}_n^{\delta}(\varepsilon_i) \tag{13}$$

Finally, we can get the semi-discrete form of the scalar advection equation on the standard element Ω_S:

$$\frac{d\hat{u}_{n,i}^d}{dt} = -\nabla_{\varepsilon} \hat{f}_n^C(\varepsilon_i) \tag{14}$$

3. A Parallel FR/CPR Solver

Based on the above formula, the algorithm flow of the FR/CPR algorithm can be obtained:

Algorithm flow of FR/CPR algorithm
for $t = 0$ **to** t_{max} **do**
Compute the flux at Solution Point
Interpolate the solution from Solution Point to Field Point
Interpolate the flux from Solution Point to Field Point
Compute the common numerical flux
Compute the derivative of the flux
Compute the derivative of reconstructed flux
Update the solution
end

We use a standard one-dimensional SOD shock tube to test the above algorithm. In this simulation, the time advancement uses SSPRK3. To avoid the influence of time advancement errors, a small time step of $\Delta t = 10^{-4}$ is adopted. Spatial discretization is based on Legendre-Gauss points, using the gDG correction function and the Roe flux, but without any shock-capturing methods, including positivity-preserving limiters, discontinuity detectors, limiters, etc.

The results are as follows:

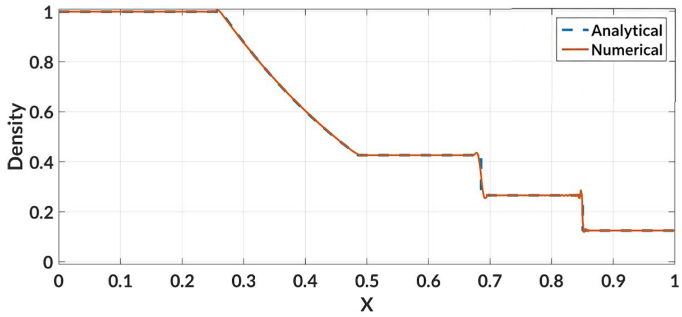

(a) Density distribution

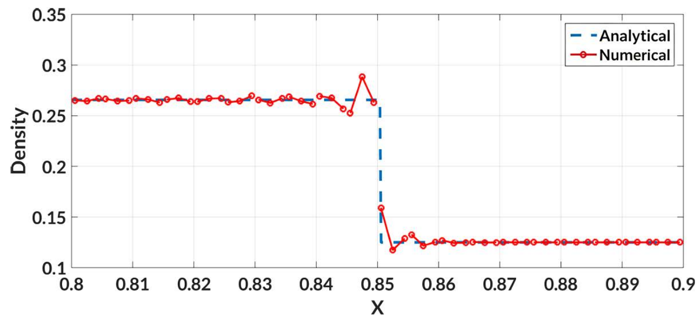

(b) Density distribution in $x \in [0.8, 0.9]$

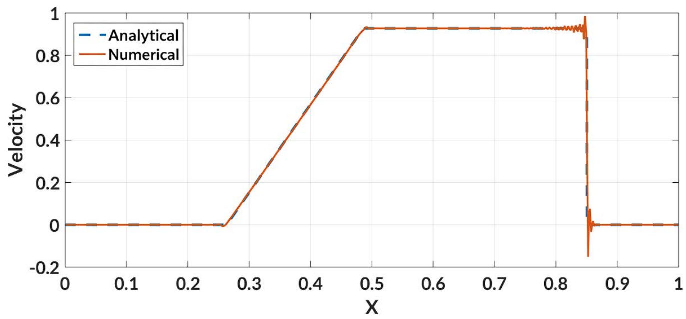

(c) Velocity distribution

Figure 1: one-dimensional SOD shock tube

Therefore, the Gibbs phenomenon generated by high-order polynomials near the discontinuity can be clearly observed from the density distribution within $x \in [0.795, 0.89]$ shown in Figure 1(b) and the velocity distribution shown in Figure 1(c). However, the results in Figure 1 indicate that even without the assistance of shock-capturing methods, the FR/CPR method accurately simulates the one-dimensional SOD shock tube problem when using 600 degrees of freedom.

Then we include limiters, The procedure for applying the discontinuity detector and limiter to the FR/CPR method is shown in Figure 2, where an explicit time marching scheme is adopted. After computing the residual R at each time step and iteratively obtaining the new solution $Q^(n+1)$ for the next time step, the discontinuity detector is used to mark grid cells that contain shocks as problematic cells. In these problematic cells, a positivity-preserving limiter is applied to check whether the iterated new solution $Q^(n+1)$ contains negative density or negative pressure. If so, it is corrected to a new solution $\hat{Q}^(n+1)$ with non-negative density and pressure. Then, a limiter is used to reconstruct a new solution $\tilde{Q}^(n+1)$. If the reconstructed solution $\tilde{Q}^(n+1)$ from the limiter still contains negative density or negative pressure, the positivity-preserving limiter is applied again to modify $\tilde{Q}^(n+1)$, ensuring that the final new solution for the next time step, $\hat{\hat{Q}}^(n+1)$, has non-negative density and pressure.

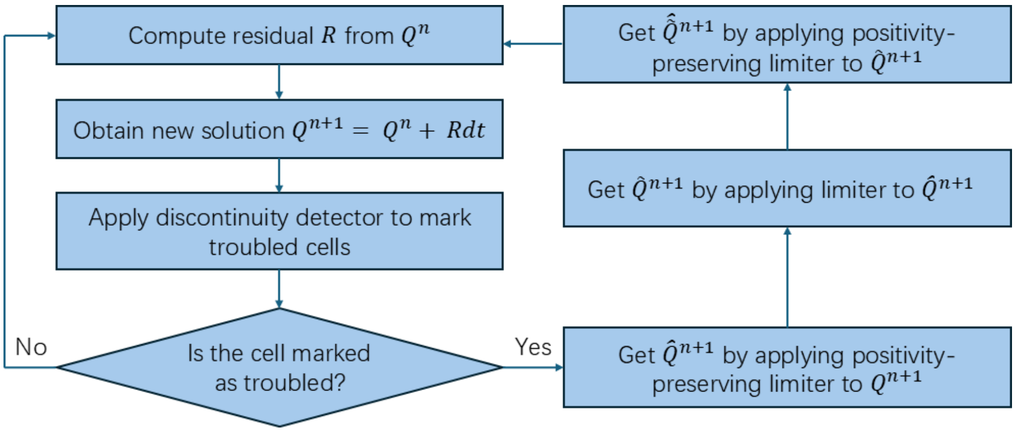

Figure 2: Flowchart of the limiter application procedure

In order to stably capture shock waves while preserving spatial accuracy as much as possible, the FR/CPR method requires a high-order limiter that maintains accuracy. Compared with classical limiters such as TVD and TVB, a high-order limiter does not compromise the accuracy of the high-order scheme even when applied to smooth solution regions without shocks. Of course, applying the limiter to smooth solution regions not only fails to improve spatial accuracy but also wastes computational resources.

We employed four different limiter to validate the accuracy and stability of the aforementioned solver using two test cases: double Mach reflection and shock–vortex interaction. The former is commonly used to evaluate the capability of high-order schemes in capturing strong shocks, while the latter is a two-dimensional unsteady inviscid flow containing discontinuities induced by shock waves. When the vortex propagates and encounters the shock, the shock structure undergoes significant distortion, generating multiple waves that propagate downstream. This case is often employed to examine how well high-order shock-capturing schemes predict the complex phenomena of vortex–shock interactions.

The double Mach reflection problem is often used in the field of numerical scheme research to test the ability of high-order schemes to capture strong shock waves. The computational domain of this two-dimensional problem is defined as $[0, 4] \times [0, 1]$. The initial conditions are set as follows: at $x = 1/6$, $y = 0$, there is a right-moving shock wave with Ma = 10, and the shock is inclined at an angle of 60° to the x-axis. The flow field upstream and downstream of the shock wave is set as follows:

$$
\begin{aligned}
(\rho, u, v, p) &= (1.4, 0, 0, 1), if\, y < \sqrt{3}(x - \frac{1}{6}) \\
(\rho, u, v, p) &= (8, 7.145, -4.125, 116.5), if\, y > \sqrt{3}(x - \frac{1}{6})
\end{aligned} \tag{15}
$$

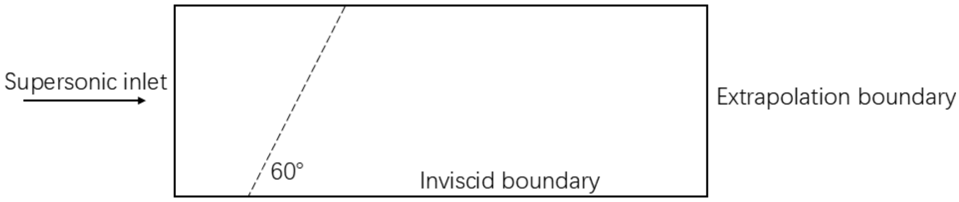

Figure 3: two-dimensional double Mach reflection problem

In two-dimensional double Mach reflection case, a simulation was conducted from the initial state to t = 0.2 seconds using 480×120 quadrilateral grids with a uniform distribution and a third-order spatial accuracy P2 scheme. For time advancement, the SSPRK3 method was employed, and a relatively small time step $\Delta t = 10^{-5}$ seconds was adopted to minimize the influence of time integration errors. Spatial discretization was based on Legendre-Gauss-Lobatto points, incorporating a gDG correction function and Roe flux. Shock-capturing approaches included TVB limiter, Modal limiter, KXRCF limiter and CKXRCF limiter. The resulting density contour distribution is shown in Figure 4. The results indicate that the FR/CPR-P2 method combined with the different limiters, based on a grid size of h=1/120, can accurately simulate strong shock waves in this case as well as the series of vortex structures formed by the roll-up of Kelvin-Helmholtz instability.

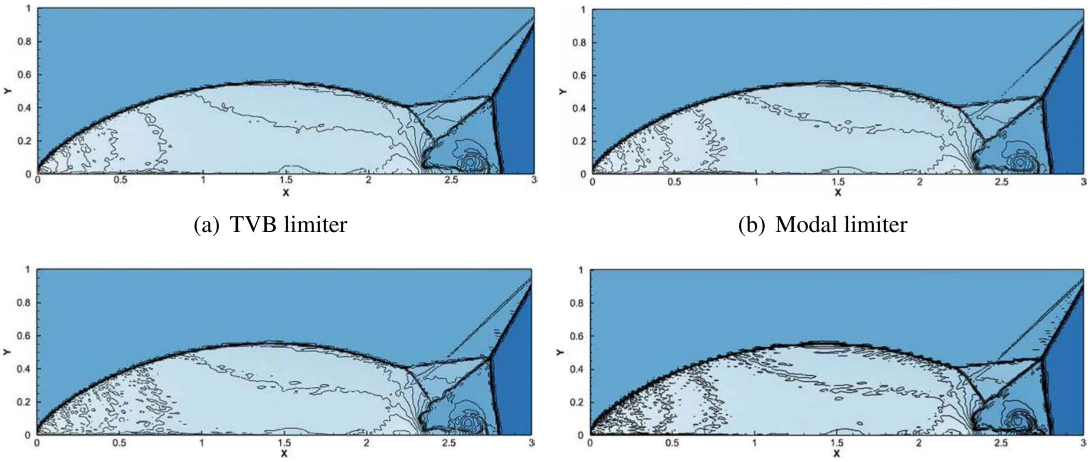

(a) TVB limiter

(b) Modal limiter

(c) KXRCF limiter

(d) CKXRCF limiter

Figure 4: Computational Results of Double Mach Reflection under Different Limiters

The results show that the four discontinuity detectors are basically accurate in marking discontinuities. CKXRCF marks the largest number of problematic grid cells, identifying shock waves, slip lines, and vortices. TVB and KXRCF are similar, marking parts of the shock waves, slip lines, and vortex regions, while the modal discontinuity detector marks only the shock waves. It is worth noting that TVB, KXRCF, and the modal discontinuity detector all fail to mark the shock waves continuously, resulting in missed problematic grid cells. Among the four discontinuity detectors, only TVB marks numerical spurious oscillations in the upstream region. Consequently, in the TVB results, the numerical spurious oscillations in the upstream region are attenuated compared to the other three results. The modal discontinuity detector does not mark the vortex region, so the vortex roll-up features are most pronounced in its results.

Overall, while the four discontinuity detectors differ in which problematic grid cells they mark, the key features of the flow field—including the shock waves, slip lines, and the series of vortex structures arising from Kelvin-Helmholtz instability roll-up—remain essentially similar.

The shock-vortex interaction problem is a two-dimensional unsteady inviscid flow containing a discontinuity caused by the shock wave. When the vortex encounters the shock wave during its propagation, the shock structure undergoes significant distortion, consequently generating multiple waves that propagate downstream. Two physical phenomena exist in this process. The first flow characteristic is that the initial vortex splits into two vortex structures due to compression effects when passing through the shock wave. The vortex structure downstream of the shock depends on the relative strength of the shock and the vortex. The second flow characteristic is the reflective propagation of wave structures downstream of the shock. The computational domain for this two-dimensional problem is defined as $[0, 2] \times [0, 1]$. The initial field contains a stationary shock wave and a vortex,

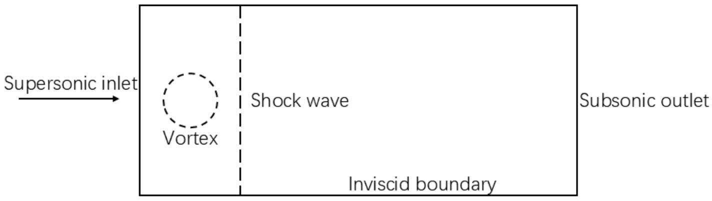

Figure 5: two-dimensional shock-vortex interaction problem

In two-dimensional shock-vortex interaction case, a simulation from the initial field to t=0.7 seconds is conducted using uniformly distributed 600×300 quadrilateral grids with fourth-order spatial accuracy based on P3 elements. For time advancement, the SSPRK3 scheme is employed, and a relatively small CFL number of 0.2 is adopted to minimize errors from time integration, resulting in a time step of approximately 2.4×10^{-5} seconds. Spatial discretization is performed on Legendre-Gauss-Lobatto points using a gDG correction function and Roe flux. Shock-capturing methods include TVB, Modal, KXRCF and CKXRCF limiter.The resulting density contour distribution is shown in Figure 6, The results demonstrate that the FR/CPR-P3 scheme combined with the P-weighted WENO limiter, using a grid size of h = 1/300, is capable of accurately simulating strong shock waves, vortex propagation, and a series of vortex structures generated by the rolling-up of the Kelvin–Helmholtz instability in this test case. However, it can also be observed that spurious oscillations still exist in the region downstream of the shock.

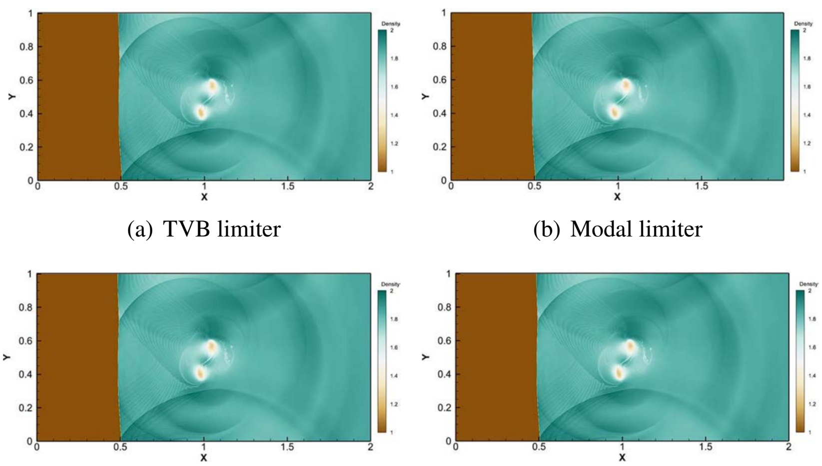

(a) TVB limiter

(b) Modal limiter

(c) KXRCF limiter

(d) CKXRCF limiter

Figure 6: Computational Results of Shock-vortex Interaction under Different Limiters

The results show that the four discontinuity detectors are generally accurate in marking discontinuities. CKXRCF only marks the shock wave, and the marked problematic grid cells are continuous. KXRCF is similar to CKXRCF, but marks slightly fewer problematic grid cells at the shock wave. TVB marks the smallest number of discontinuous shock wave regions as problematic grid cells. The modal discontinuity detector, similar to CKXRCF and KXRCF, marks continuous shock wave regions as problematic grid cells. However, TVB and the modal discontinuity detector also mark a small number of vortex structures and reflected wave regions as problematic grid cells. Although the four discontinuity detectors differ in which grid cells are marked as problematic, the key features of the overall flow field are largely consistent.

4. Conclusion

This study develops an unstructured parallel solver based on the FR/CPR method and employs four limiters—TVB, Modal, KXRCF, and CKXRCF—to simulate two classic test cases: double Mach reflection and shock–vortex interaction. All four limiters successfully capture key discontinuous features in the flow field, resolve the complete shock morphology, and clearly track the multiple reflections and interactions of shocks with walls. The wave system exhibits a well-defined layered structure, and the reflection process of the shock system is distinctly visible. The resulting flow field structures are clear and the captured features are complete.

References

[1] Z. Wang, Krzysztof Fidkowski, Rémi Abgrall, Francesco Bassi, Doru Caraeni, Andrew Cary, H. Deconinck, Ralf Hartmann, Koen Hillewaert, H.T. Huynh, Norbert Kroll, Georg May, Per-Olof Persson, Bram van Leer, and Miguel Visbal. High-order cfd methods: Current status and perspective. *International Journal for Numerical Methods in Fluids*, 72:811–845, 01 2013.

[2] F. Bassi and S. Rebay. A high-order accurate discontinuous finite element method for the numerical solution of the compressible navier–stokes equations. *Journal of Computational Physics*, 131(2):267–279, 1997.

[3] David A. Kopriva. A staggered-grid multidomain spectral method for the compressible navier–stokes equations. *Journal of Computational Physics*, 143(1):125–158, 1998.

[4] Yen Liu, Marcel Vinokur, and Z.J. Wang. Spectral difference method for unstructured grids i: Basic formulation. *Journal of Computational Physics*, 216(2):780–801, 2006.

[5] Z.J. Wang and Yen Liu. Spectral (finite) volume method for conservation laws on unstructured grids: Ii. extension to two-dimensional scalar equation. *Journal of Computational Physics*, 179(2):665–697, 2002.

[6] Z.J. Wang. High-order methods for the euler and navier–stokes equations on unstructured grids. *Progress in Aerospace Sciences*, 43(1):1–41, 2007.

[7] H.T. Huynh. A flux reconstruction approach to high-order schemes including discontinuous galerkin methods. *AIAA Paper AIAA 20074079*, pages 1–42, 01 2007.

[8] Laiping Zhang, Liu Wei, He Lixin, Deng Xiaogang, and Zhang Hanxin. A class of hybrid dg/fv methods for conservation laws i: Basic formulation and one-dimensional systems. *Journal of Computational Physics*, 231(4):1081–1103, 2012.

[9] Takanori Haga, Haiyang Gao, and Z. Wang. A high-order unifying discontinuous formulation for 3-d mixed grids. *AIAA paper*, 540:2010, 01 2010.

[10] Z.J. Wang and Haiyang Gao. A unifying lifting collocation penalty formulation including the discontinuous galerkin, spectral volume/difference methods for conservation laws on mixed grids. *Journal of Computational Physics*, 228(21):8161–8186, 2009.

[11] H.T. Huynh, Z.J. Wang, and P.E. Vincent. High-order methods for computational fluid dynamics: A brief review of compact differential formulations on unstructured grids. *Computers & Fluids*, 98:209–220, 2014. 12th USNCCM mini-symposium of High-Order Methods for Computational Fluid Dynamics - A special issue dedicated to the 80th birthday of Professor Antony Jameson.